Atmos. Chem. Phys. Discuss., 15, 9405–9443, 2015
www.atmos-chem-phys-discuss.net/15/9405/2015/
doi:10.5194/acpd-15-9405-2015

Atmospheric Chemistry and Physics Discussions

Size-resolved source apportionment of particulate matter in urban Beijing during haze and non-haze episodes

S. L. Tian, Y. P. Pan, and Y. S. Wang

State Key Laboratory of Atmospheric Boundary Layer Physics and Atmospheric Chemistry (LAPC), Institute of Atmospheric Physics, Chinese Academy of Sciences, Beijing 100029, China

Received: 14 January 2015 – Accepted: 25 February 2015 – Published: 30 March 2015

Correspondence to: Y. S. Wang (wys@mail.iap.ac.cn)
and Y. P. Pan (panyuepeng@mail.iap.ac.cn)

Published by Copernicus Publications on behalf of the European Geosciences Union.

Abstract

More size-resolved chemical information is needed before the physicochemical characteristics and sources of airborne particles can be understood, but this information remains unavailable in most regions of China due to a paucity of measurement data. In this study, we report a one-year observation of various chemical species in size-segregated particle samples collected in urban Beijing, a mega city that experiences severe haze episodes. In addition to fine particles, the measured particle size distributions showed high concentrations of coarse particles during the haze periods. The abundance and chemical compositions of the particles in this study were temporally and spatially variable, with major contributions from organic matter and secondary inorganic aerosols. The contribution of the organic matter to the mass decreased from 37.9 to 33.1 %, whereas the total contribution of SO_4^{2-}, NO_3^- and NH_4^+ increased from 19.1 to 32.3 % on non-haze and haze days, respectively. Due to heterogeneous reactions and hygroscopic growth, the peaks in the size distributions of organic carbon, SO_4^{2-}, NO_3^-, NH_4^+, Cl^-, K^+ and Cu shifted from 0.43–0.65 µm on non-haze days to 0.65–1.1 µm on haze days. Although the size distributions are similar for the heavy metals Pb, Cd and Tl during the observation period, their concentrations increased by a factor of more than 1.5 on haze days compared with non-haze days. We found that NH_4^+ with a size range of 0.43–0.65 µm, SO_4^{2-} and NO_3^- with a size range of 0.65–1.1 µm and Ca^{2+} with a size range of 5.8–9 µm as well as the meteorological factors of relative humidity and wind speed were responsible for the haze pollution when the visibility was less than 15 km. Source apportionment using positive matrix factorization identified six common sources: secondary inorganic aerosols (26.1 % for fine particles vs. 9.5 % for coarse particles), coal combustion (19 vs. 23.6 %), primary emissions from vehicles (5.9 vs. 8.0 %), biomass burning (8.5 vs. 2.9 %), industrial pollution (6.3 vs. 8.5 %) and mineral dust (16.1 vs. 35.1 %). The first four factors were higher on haze days, while the latter factors were higher on non-haze days. The sources generally increased with decreasing size with the exception of mineral dust. However, two peaks were consis-

ACPD
15, 9405–9443, 2015

tently found in the fine and coarse particles. The contributing sources also varied with the wind direction; coal and oil combustion products increased during southern flows, indicating that any mitigation strategy should consider the wind pattern, especially during the haze periods. The findings indicated that the $PM_{2.5}$-based dataset is insufficient for the Chinese source control policy, and detailed size-resolved information is urgently needed to characterize the important sources in urban regions and better understand severe haze pollution.

1 Introduction

Particulate matter (PM) is among the most important atmospheric pollutants that negatively affect human health and visibility. In addition, PM plays a significant role in global climate and ecosystem cycling (Huang et al., 2014; McFiggans, 2014; Pan et al., 2013). Due to rapid industrialization and urbanization in recent decades, China has become one of the most significant source regions for anthropogenic emissions to the atmosphere in the world (Guo et al., 2014). The Chinese capital of Beijing, a megacity with approximately 21 million inhabitants (Beijing statistical yearbook 2013), is experiencing extreme haze events (Sun et al., 2004; Li et al., 2013; Du et al., 2014). Although previous studies have provided valuable information on the physical and chemical characteristics of PM in urban Beijing and the surrounding areas (Song et al., 2006; Chan et al., 2005; Schleicher et al., 2013), haze formation remains unclear due to its complexity (Yang et al., 2014; Jing et al., 2014). In addition, previous studies have primarily focused on single particle fractions, such as $PM_{2.5}$, and have neglected size-resolved chemical information, especially for coarse particles, which also play an important role in haze events (Tian et al., 2014; Sun et al., 2013).

Knowing the size distributions and associated chemical species is crucial for the evaluation of the effects of PM on human health, visibility, and regional radiative forcing, as well as the determination of the sources, formation mechanisms and conversion processes of the particles (Pillai and Moorthy, 2001; Duarte et al., 2008; Liu et al.,

ACPD
15, 9405–9443, 2015

2008; Contini et al., 2014). Recent results have suggested that secondary sulfates and nitrates primarily form fine particles, with elevated concentrations in the droplet mode during haze days (Sun et al., 2013; Wang et al., 2012). During the extreme haze events in urban Beijing in early 2013, the peak mass concentration of particles shifted from 0.43–0.65 µm on clear days to 0.65–1.1 µm on lightly polluted days and to 1.1–2.1 µm on heavily polluted days due to hygroscopic growth of submicron particles and the formation of secondary particles, including organic carbon (OC), NH_4^+, SO_4^{2-} and NO_3^- (Tian et al., 2014). Due to the paucity of long-term observations, it remains unclear whether the peak shifts can be observed during other periods or whether this phenomenon only occurred in the extreme haze events in early 2013. In addition, source apportionment based on size-fractionated PM data would provide additional insight into aerosol sources, especially during haze events (Pant and Harrison, 2012). For example, receptor models have been successfully used to identify coarse aerosol sources separately from fine aerosol sources (Karanasiou et al., 2009; Titos et al., 2014). Previous studies regarding size distributions of PM in urban Beijing have primarily focused on limited chemical species (Sun et al., 2013; Li et al., 2013; Yao et al., 2003) or have been conducted over short periods (Li et al., 2012b; Sun et al., 2010; Gao et al., 2012; Zhang et al., 2014). To the best of our knowledge, no studies have been conducted on source apportionment of size-resolved atmospheric particles based on long-term observations in urban Beijing.

To fill these gaps, we began a one-year observation of size-resolved PM in urban Beijing from 1 March 2013 to 28 February 2014. In this study, we report the mass closure of particles based on a size-resolved chemical dataset on haze and non-haze days over four seasons. Positive matrix factorization (PMF) combined with back trajectory cluster analysis was applied to estimate the relative contributions of sources in different size fractions between haze and non-haze days and among different regional sources. These results will help policy-makers design emission control strategies and can serve as a database for future field measurements and modeling studies.

ACPD
15, 9405–9443, 2015

2 Materials and methods

2.1 Sampling site

The experiment was performed from 1 March 2013 to 28 February 2014 at the Institute of Atmospheric Physics, Chinese Academy of Sciences (39°58′ N, 116°22′ E). The samplers were placed on the roof of a building, which is approximately 15 m above the ground. The sampling site was located in Northwest Beijing and situated between the 3rd and 4th ring roads. The site was selected to be broadly representative of air pollution level in urban Beijing as it was far from specific point emission sources.

2.2 Sampling collection

Two 9-stage samplers (Andersen Series 20–800, USA) with cutoff points of 0.43, 0.65, 1.1, 2.1, 3.3, 4.7, 5.8, and 9.0 µm, were used to simultaneously collect particles for 48 h from 10:00 local time (LT) on Monday to 10:00 LT on Wednesday every week at a flow rate of 28.3 L min^{-1}. In total 52 sets of size-resolved PM samples were collected on quartz fiber filters and the cellulose membranes (81 mm in diameter) during the study period, respectively. The quartz fiber filters were pre-fired (2 h at 800 °C) to remove all organic material, and were weighed before and after sampling by a microbalance with balance sensitivity ±0.01 mg. Filters were conditioned in a dryer with temperature of 25 ± 3 °C and relative humidity (RH) of 10 ± 2 % for 72 h before each weighing. After re-weighing, the exposed filters were stored in a freezer at −20 °C to limit losses of volatile components loaded on the filters. Meanwhile, the meteorological parameters used in this study, including visibility, temperature, RH, wind speed (WS) and wind direction (WD), were collected at Beijing Capital International Airport (http://english.wunderground.com).

ACPD
15, 9405–9443, 2015

2.3 Chemistry analyses

A quarter of each quartz filter was extracted using 25 mL of deionized water (Millipore, 18.2 MΩ) and an ultrasonic bath for 30 min. The extraction liquid was filtered and subsequently measured by ion chromatograph (DIONEX, ICS-90, USA) for the concentrations of Na^+, NH_4^+, K^+, Mg^{2+}, Ca^{2+}, Cl^-, NO_3^- and SO_4^{2-}. After another quarter of each quartz filter was cut, the concentrations of OC and elemental carbon (EC) were determined by using a thermal/optical carbon aerosol analyzer (DRI Model 2001A, Desert Research Institute, USA).

A quarter of the cellulose membrane was digested in a mixture of concentrated HNO_3 (6 mL), HCl (2 mL) and HF (0.2 mL) with a closed vessel microwave digestion system (MARS5, CEM Corporation, Matthews, NC, USA). Then, Agilent 7500a inductively coupled plasma mass spectrometry (ICP-MS, Agilent Technologies, Tokyo, Japan) was used to determine the concentrations of 21 trace elements (TEs) (Na, Mg, Al, K, Ca, V, Cr, Mn, Fe, Co, Ni, Cu, Zn, As, Mo, Cd, Ba, Tl, Pb, Th and U). The analysis methods and the information about the instruments used in this study (e.g., precision, calibration and detection limit) as well as quality control work were given elsewhere (Pan and Wang, 2015; Li et al., 2012a).

2.4 Chemical mass closure

Mass closure was examined to discuss the relative contributions of the major components in PM. The chemical species were divided into the following seven categories. i.e., sulfate-nitrate-ammonium (SNA), organic matter (OM), crustal materials (CM), heavy metals (HM), EC, sea salt (SS) and liquid water (LW). The difference between the mass weighted by microbalance and that reconstructed by the above seven components was defined as unidentified matter (UM). The calculation methods of the main components were described in our previous studies (Tian et al., 2014) and are shown in Table S1 in the Supplement for the readers' convenience.

ACPD
15, 9405–9443, 2015

2.5 PMF model

PMF is an effective source apportionment receptor model (Karanasiou et al., 2009; Bullock et al., 2008). In this study, EPA-PMF 3.0 was applied separately to each size fraction (< 0.43, 0.43–0.65, 0.65–1.1, 1.1–2.1, 2.1–3.3, 3.3–4.7, 4.7–5.8, 5.8–9 and > 9 µm), and further $PM_{2.1}$ and $PM_{2.1-9}$. The input data included concentrations of mass, Na, Mg, Al, K, Ca, V, Cr, Mn, Fe, Co, Ni, Cu, Zn, As, Mo, Cd, Ba, Tl, Pb, Th, U, Na^+, NH_4^+, K^+, Mg^{2+}, Ca^{2+}, Cl^-, SO_4^{2-}, NO_3^-, OC, EC and the uncertainty of the data, which can be calculated as below:

If the concentration is less than or equal to the method detection limit (MDL) provided, the uncertainty is calculated using the following equation:

$$\text{Uncertainty} = 5/6 \times \text{MDL} \quad (1)$$

If the concentration is greater than the MDL provided, the calculation is

$$\text{Uncertainty} = \sqrt{(\text{Error Fraction} \times \text{concentration})^2 + (\text{MDL})^2} \quad (2)$$

In this study, error fraction was estimated as 10 (the percent uncertainty multiplied by 100) for all the chemical species and MDL were similar with that reported in previous studies (Li et al., 2012b; Yang et al., 2009).

The base model was run 20 times with different numbers of factors to get the best possible solution. In the first run, several species had a large number of absolute scaled residuals greater than 3, indicating poor observed-predicted correlations. Then, these species were designated "weak" and the model was rerun. When a reasonable solution was found, bootstrapping technique has been used to obtain the most meaningful results. A total of 100 bootstrap runs were performed with a minimum r^2 value of 0.6. Of the 100 runs, the 6-factors were mainly mapped to a base factor in every run indicating a stable result.

There are several important criteria to ensure a good PMF solution. First of all, the modeled Q's should be within 50 % of the theoretical value. Secondly, the optimum

ACPD
15, 9405–9443, 2015

number of factors is determined by the criterion that each factor has distinctively dominant grouping of compounds. Thirdly, the model uncertainty produced by bootstrapping should be small. The principles can be found elsewhere in detail (Liu et al., 2014; Titos et al., 2014; Moon et al., 2008).

2.6 Air mass back trajectory cluster

Three-day backward trajectories arriving at the sampling site were calculated using the National Oceanic and Atmospheric Administration (NOAA) HYSPLIT 4 model with a 0.5° × 0.5° latitude–longitude grid. The arrival level was set at 500 m a.g.l. The HYSPLIT model was run four times per day at starting times of 02:00, 08:00, 14:00, and 20:00 UTC during the whole sampling period. Then, all the trajectories were divided into different groups based on horizontal moving speed and direction of air masses to form the trajectory clusters (Sirois and Bottenheim, 1995; Wang et al., 2006).

3 Results

3.1 Abundance and compositions

Table 1 describes the concentrations of the size-resolved mass and chemical compositions in different seasons. It was found that the annual average concentrations of $PM_{2.1}$ and PM_9 were 67.3 and 129.6 $\mu g\,m^{-3}$, respectively. Although the present level of $PM_{2.1}$ is significantly lower than that in 2009–2010 (135 $\mu g\,m^{-3}$) (R. Zhang et al., 2013), it was over three times higher than the National Ambient Air Quality Standard (NAAQS), which specifies an annual average $PM_{2.5}$ of 15 $\mu g\,m^{-3}$ (GB3095-2012, Grade I). In addition, PM_9 was approximately three times the NAAQS annual average PM_{10} of 40 $\mu g\,m^{-3}$ (Grade I). Thus, fine and coarse particles, defined in this study as particles with size < 2.1 and 2.1–9.0 µm, respectively, are important for the PM in urban Beijing.

ACPD
15, 9405–9443, 2015

As shown in Table 1, the primary components of $PM_{2.1}$ are OC (24.5 % of $PM_{2.1}$), SO_4^{2-} (14.7 %), NO_3^- (11.2 %) and NH_4^+ (9.2 %). In contrast, Ca ($3.5 \pm 1.5\,\mu g\,m^{-3}$), EC ($2.0 \pm 1.8\,\mu g\,m^{-3}$) and other species accounted for approximately 40 % of $PM_{2.1}$.The composition of coarse particles was different from that of fine mode. In this study the highest contribution to $PM_{2.1-9}$ was Ca (16.3 % of $PM_{2.1-9}$), followed by OC (15.5 %), NO_3^- (4.5 %), Fe (4.1 %) and SO_4^{2-} (3.5 %). These species in total accounted for about 44 % of $PM_{2.1-9}$. The mass closure of size-resolved particles will be discussed in detail below (Sect. 4.2).

3.2 Seasonality

The concentrations of $PM_{2.1}$ were highest in winter (December to February, $76.8\,\mu g\,m^{-3}$), followed by spring (March to May), summer (June to August) and autumn (September to November), with concentrations around $65\,\mu g\,m^{-3}$ in the latter three seasons (Table 1). In contrast, the concentrations of $PM_{2.1-9}$ followed the order of spring > autumn > winter > summer.

The seasonal dependency varied by species. For most of the species that were enriched in the fine mode (with a $PM_{2.1}$ / PM_9 chemical concentration ratio greater than 0.5, including NH_4^+, Tl, Cd, Pb, SO_4^{2-}, NO_3^-, EC, K^+, V, Zn, Cr, Cl^-, OC, Cu, As, Na, Na^+, Mo and K), their concentrations in $PM_{2.1}$ and $PM_{2.1-9}$ exhibited similar seasonal variations, with the $PM_{2.1}$ mass concentration being higher during colder seasons. However, the seasonal dependence of the concentration of certain species in $PM_{2.1}$ differs from the typical seasonal variation. For example, the concentrations of SO_4^{2-} and NH_4^+ in spring and summer were higher than those in autumn and winter. This result was consistent with the seasonal variability of SO_4^{2-} and NH_4^+ in $PM_{2.5}$ in 2009–2010 (R. Zhang et al., 2013).

In addition, the OC in $PM_{2.1}$ exhibited a seasonal pattern of waxing in summer and waning in autumn. The high OC concentration in summer was primarily a result of the photochemistry generating more secondary organic carbon (SOC). This result can be

ACPD
15, 9405–9443, 2015

confirmed by the OC / EC ratios, which are higher in summer (13.7) than autumn (6.8). As EC primarily arises from primary combustion emissions, the OC / EC ratios were used to evaluate the contribution from secondary organic carbons (Cao et al., 2007).

For species enriched in the coarse mode (with a $PM_{2.1}$ / PM_9 chemical concentration ratio below 0.5, including Ni, Mn, U, Co, Mg^{2+}, Th, Al, Ba, Mg, Ca and Ca^{2+}), their concentrations in $PM_{2.1}$ and $PM_{2.1-9}$ demonstrated a typical seasonal variation, with higher concentrations observed in spring and autumn (or winter) due to the influence of re-suspended soil dust.

3.3 Size distribution

The size distributions of the mass concentrations and the chemical species are shown in Fig. 1. In each season, the size distribution of the mass concentrations was bimodal. The fine modes commonly showed maxima at 0.65–1.1 µm in spring, autumn and winter but 0.43–0.65 µm in summer. The coarse modes showed maxima at 4.7–5.8 µm in all of the seasons. As shown in Fig. 1, the peak of the fine mode was broader in winter than in the other seasons, indicating the complexity of the emissions in winter (Sun et al., 2013).

The chemical species can generally be divided into three groups based on their size distributions. First, SO_4^{2-}, NO_3^-, NH_4^+, EC, Zn, Cd, Pb and Tl were abundant in the fine mode, which exhibited maxima at 0.43–0.65 or 0.65–1.1 µm in all four seasons, corresponding to coal and motor vehicle sources (Li et al., 2013). Second, Ca^{2+}, Mg^{2+}, Ba, Mg, Al, Ca, Fe, Co, Ni, Th and U were primarily concentrated in the coarse mode from 4.7 to 5.8 µm, which suggests natural sources from soil dust or mechanical abrasion processes (Sun et al., 2013; Maenhaut et al., 2002). Third, OC, Cl^-, K^+, Na^+, Na, K, V, Cr, Mn, Cu, As and Mo exhibited typical bimodal distributions, and the amplitude of the fine mode correlated well with that of the coarse mode. These species exhibited maxima at 0.43–0.65 or 0.65–1.1 µm and peaked at 4.7–5.8 µm in the coarse mode. These

ACPD
15, 9405–9443, 2015

species may represent biomass burning sources, as Cl^- and K^+ are good biomass burning tracers (Du et al., 2011), and industrial pollution.

The size distribution of the mass concentration and OC peaked at 0.43–0.65 µm in summer but 0.65–1.1 µm in winter. Because the primary organic carbon emissions were relatively stable over the four seasons, the size distribution differences in the fine mode were primarily due to the SOC generation (Duan et al., 2005). The difference between summer and winter indicated that the SOC formation in summer was enhanced due to photochemical reactions and primarily accumulated in "condensation mode" (Zhang et al., 2008). However, because photochemistry is typically weak in winter, the SOC generation was primarily due to the high RH as well as a high concentration of precursors; thus, it primarily accumulated in "droplet mode" (Cao et al., 2007). Our previous findings indicate that the weakening of the incident solar radiation reduces the SOC formation in the smaller size fraction, whereas the high RH plays an important role in the SOC generation in the larger size fraction (Tian et al., 2014).

4 Discussion

4.1 Size-resolved aerosol compositions on non-haze and haze days

Figure 2 illustrates the size-segregated PM mass concentrations during the sampling period. As shown, non-haze days (average visibility > 10 km) and haze days (average visibility < 10 km) were observed in all four seasons. During the observation period, 12 sets of size-resolved PM samples were collected during non-haze days and 25 sets during haze days (marked in Fig. 2). The remaining 15 sets that collected during extreme weather events (i.e., rain, snow or fog) were excluded from the dataset.

ACPD
15, 9405–9443, 2015

4.1.1 Concentration enhancement ratios

Table S2 describes the annual average concentrations of the size-resolved mass and chemical compositions on haze and non-haze days over four seasons. The annual average $PM_{2.1}$ and $PM_{2.1-9}$ concentrations on haze days were 78.4 and 70.1 $\mu g\,m^{-3}$, which were 2.4 and 1.4 times those on non-haze days, respectively. Therefore, it is evident that fine particles accumulated markedly during the haze pollution period (Wang et al., 2014). In addition, the mass concentration enhancement ratio from non-haze to haze days ($R_{H/N}$) in all four seasons was examined. The $R_{H/N}$ for fine particles revealed a typical seasonality, with the highest value in winter (4.6) and the lowest value in spring (1.5). The $R_{H/N}$ for coarse particles was lower than that for fine particles, which ranged from 1.0 to 1.9, and followed the order of summer > autumn > winter > spring. The higher $R_{H/N}$ values for fine particles further indicated the importance of fine particles in haze pollution.

The annual average $R_{H/N}$ of the chemical components in $PM_{2.1}$ ranged from 0.8 to 4.7, with values above 2.4 for NO_3^-, SO_4^{2-}, NH_4^+, Pb, Cl^-, Tl and Cd. This finding was consistent with those in previous studies (Tian et al., 2014; Sun et al., 2013), indicating that coal and motor vehicle sources played important roles in haze pollution (Li et al., 2013). Regarding the seasonal variations, the particulate mass and most of the species exhibited the highest $R_{H/N}$ in winter, which indirectly showed that severe haze events primarily occurred in winter.

Simultaneously, the annual average $R_{H/N}$ of the chemical components in $PM_{2.1-9}$ ranged from 0.4 to 4.5, which was close to that for fine particles. NO_3^-, SO_4^{2-}, NH_4^+, Pb, Cl^-, Tl, Cd, EC, Na^+, K^+, OC, Mo and Zn in the coarse fraction exhibited $R_{H/N}$ values greater than 1.4. These species had the highest toxicity. Thus, the mitigation of particles with diameters greater than 2.1 µm cannot be neglected during haze events. Similar to $PM_{2.1}$, most of the species in the coarse fraction exhibited the highest $R_{H/N}$ in winter. In contrast, the highest $R_{H/N}$ for Na^+, K^+ and Cl^- in the coarse fraction was observed in summer, which is similar to that of the mass concentration.

ACPD
15, 9405–9443, 2015

It is interesting to note that the concentrations of NO_3^-, SO_4^{2-} and NH_4^+ in the fine and coarse particles were higher on haze days than on non-haze days. These species are involved in the heterogeneous chemical reactions (Sun et al., 2013). Figure S2a and b shows good correlations between NH_4^+ and SO_4^{2-} in fine particles for non-haze and haze days, with an NH_4^+ / SO_4^{2-} molar ratio greater than unity (ranging from 1.2–1.4), revealing the dominance of $(NH_4)_2SO_4$. We further calculated the molar ratio of NH_4^+ to $[NO_3^- + SO_4^{2-}]$ (Fig. S2c and d), which was slightly higher than unity on non-haze days, indicating the presence of NH_4NO_3 in the fine mode aerosols. However, on haze days, the ratios were less than unity, indicating that NO_3^- may be present in chemical forms other than NH_4NO_3.

4.1.2 Peak shifts

Figure 3 compares the annual average mass concentration size distributions on non-haze and haze days, which were considered to be bimodal, with the peaks corresponding to the fine modes located at 0.65–1.1 µm and those corresponding to the coarse modes peaking at 4.7–5.8 µm. No significant differences in the average size distributions were found between haze and non-haze days in each season (Fig. 3). This result was inconsistent with that for early 2013, which showed that the peak mass concentration of fine mode particles shifted from 0.43–0.65 µm on clear days to 0.65–1.1 µm on lightly polluted days and 1.1–2.1 µm on heavily polluted days (Tian et al., 2014).

However, in this study, peak shifts from 0.43–0.65 µm on non-haze days to 0.65–1.1 µm on haze days were observed in the annual average size distributions of SO_4^{2-}, OC, NO_3^-, NH_4^+, Cl^-, K^+ and Cu. The peak values of these species at 0.43–0.65 µm in the fine mode on non-haze days correspond to the "condensation mode" due to the transformation of precursors and heterogeneous reactions, while those at 0.65–1.1 µm on haze days correspond to the "droplet mode", which likely form in clouds or through aqueous-phase chemical reactions (Sun et al., 2013). The high RH during haze days may facilitate the formation of "droplet mode" particles, and a similar finding has

ACPD
15, 9405–9443, 2015

been previously reported (Sun et al., 2013; G. Zhang et al., 2013). However, this result was slightly different from that observed in early 2013, which showed that the peak concentration of NH_4^+, SO_4^{2-} and NO_3^- in fine mode at 1.1–2.1 µm on heavily polluted days was due to the high RH and high concentrations of precursors (Tian et al., 2014).

4.2 Mass closure studies

4.2.1 Non-haze vs. haze days

Mass closure studies show that SNA, OM and CM dominated the fine particles, which accounted for 87.7 and 77.2 % of the $PM_{2.1}$ mass on non-haze and haze days, respectively (Fig. 4a–d). Generally, the contributions of OM to $PM_{2.1}$ were greater than those from SNA and CM. However, during haze episodes in cold seasons, SNA was more significant than OM because the high RH and higher precursor emissions (i.e., SO_2) promoted the generation of SNA (Tian et al., 2014). The contribution of SNA to the fine particle mass was significantly higher on haze days than on non-haze days. In contrast, the CM and OM contributions decreased from non-haze to haze days.

High total CM, OM and SNA contributions were also observed in $PM_{2.1-9}$, accounting for 58.3 and 55.1 % of the total $PM_{2.1-9}$ mass on non-haze days and haze days, respectively. The contributions of these species followed the order of CM > OM > SNA. Simultaneously, SNA and CM exhibited a variation similar to that of $PM_{2.1}$ from non-haze to haze days.

4.2.2 Differences among size fractions

For different size fractions, the contributions of OM, HM and EC were maximal in the < 0.43 µm fraction (41.3, 2.2 and 7.0 %, respectively). These fractions are related to the primary emissions of PM. The contribution of SNA, which is primarily formed from their precursors via heterogeneous reactions, was maximal in the 0.43–0.65 µm fraction (34.5 %), which is within the "condensation mode" (Fig. 4e). The contribution de-

ACPD
15, 9405–9443, 2015

creased as the size increased, indicating that these anthropogenic species primarily accumulated in the fine mode. However, the minimal contributions of OM, HM, EC and SNA were observed for the sizes 5.8–9 (6.9 %), > 9 (0.7 %), 4.7–5.8 (0.9 %) and > 9 µm (4.1 %), respectively. In addition, CM and SS shared a similar size fraction variation, which increased from < 0.43 to 3.3–4.7 µm and then decreased. The highest contributions of CM and SS appeared in the 3.3–4.7 µm fraction, being 35.6 and 4.9 %, respectively.

4.2.3 Unidentified mass

The reconstructed PM mass concentrations were compared with the gravimetric values, as shown in Fig. S3. The results were well correlated with one another in different size fractions, with R^2 values for $PM_{1.1}$, $PM_{2.1}$, PM_9 and TSP of 0.69, 0.79, 0.70 and 0.60, respectively. In addition, the contributions of the unidentified components ranged from 0.4 to 57.8 % and increased as the sizes increased. The large unidentified components in the coarse particles may be due to the underestimation of CM (Hueglin et al., 2005; Sun et al., 2004). In this study, Si was estimated as 3.42 times Al, and the ratios were applied to all of the size fractions. This assumption may be underestimated because the Si / Al ratio could increase with the size. For example, the contribution of CM to coarse particles reached 42.4 % based on the Si / Al ratio in $PM_{2.5-10}$ of 6.0, which was previously reported in Beijing (Zhang et al., 2010). Then, the contribution of the unidentified components decreased from 38.5 to 25.5 % for the total $PM_{2.1-9}$ mass.

4.3 Source apportionment

4.3.1 Fine and coarse particles

Six sources were identified using PMF analysis for the fine and coarse fractions (Fig. 5): secondary inorganic aerosol (SIA), coal combustion, primary emissions from vehicles,

ACPD
15, 9405–9443, 2015

industrial pollution, biomass burning and mineral dust. These sources represented 82.1 and 87.7 % of $PM_{2.1}$ and $PM_{2.1-9}$, respectively.

The first source is relevant to SIA, which is typically characterized by significant amounts of SO_4^{2-}, NO_3^- and NH_4^+. SIA contributed 26.1 (17.5 $\mu g\,m^{-3}$) and 9.5 % (5.9 $\mu g\,m^{-3}$) to the fine particles and coarse particles, respectively. The SIA contribution to the fine particles was similar to that in Beijing for 2009–2010 (R. Zhang et al., 2013).

The second source, coal combustion, is characterized by elevated As associated with high OC, EC, SO_4^{2-}, Pb and Zn (Tian et al., 2010; Kang et al., 2011). The contribution of this source to $PM_{2.1}$ was 19.6 % (13.2 $\mu g\,m^{-3}$), which closely approximates the value of 19 % derived in Beijing for 2009–2010 (R. Zhang et al., 2013). In addition to its contribution to $PM_{2.1}$, coal combustion significantly contributed to $PM_{2.1-9}$ (23.6 %, 14.7 $\mu g\,m^{-3}$).

The third source is primary emissions from vehicles, which are characterized by high EC, NO_3^-, Fe, Zn, Cu, Mn and Pb (Begum et al., 2004; Karnae and John, 2011). EC primarily arises from engines; Fe and Zn are found in tailpipe emissions; Cu, Fe, Mn and Pb typically exist in brake wear dust, and Pb is present in motor and fuel oil combustion (Yang et al., 2013). This source explained 5.9 % of $PM_{2.1}$ and 8.0 % of $PM_{2.1-9}$. During 2000 and the period 2009–2010, the contributions from vehicles to the fine particles in Beijing were 7 and 4 %, respectively (Zheng et al., 2005; R. Zhang et al., 2013), and these values were close to those reported in this study. In addition to primary emissions, vehicles also emit large amounts of NO_x precursors, which contributed significantly to the PM via the generation of secondary particles. This important contribution was included in the SIA source but not in the primary emissions factor due to the limitations of the PMF method. Thus, the contributions of traffic emissions to PM will be much higher than the present value if we further consider the secondary formation of NO_3^- from NO_x.

ACPD
15, 9405–9443, 2015

The fourth source is industrial pollution, which is characterized by high OC, V, Cr, Cu and Zn contents (Karnae and John, 2011). The contribution from this source was 6.3 %, which is slightly lower than the 8.5 % contribution for coarse particles.

The fifth source, biomass burning, is represented by high K contents (also K^+, which is an excellent tracer of aerosols from biomass burning) and is rich in OC and Cl^- (Moon et al., 2008). The contribution in $PM_{2.1}$ was 8.5 %, which was significantly higher than the 2.9 % contribution in $PM_{2.1-9}$. This finding is expected because biomass burning contributed much more to the fine particles than the coarse particles (Cheng et al., 2014).

The sixth component, mineral dust, is related to the high loading of crustal elements, such as Al, Ca (Ca^{2+}), Fe, Mg (Mg^{2+}), K (K^+) and OC (Titos et al., 2014; Vecchi et al., 2008). This source might indicate local and long-range transported dust aerosols and represents 16.1 and 35.1 % of the total mass in the fine and coarse fractions, respectively. This high contribution of the mineral source to the fine fraction was similar to the results for Beijing during 2009–2010 (R. Zhang et al., 2013).

4.3.2 Non-haze vs. haze days

Figure 6a–d illustrates the contributions of the six sources to the fine and coarse particles on clear and haze days. On haze days, the contributions of SIA, coal combustion, primary emissions from vehicles, industrial pollution, biomass burning and mineral dust were 24.9, 19.9, 7.9, 5.4, 8.6, and 10.3 % to the fine fractions and 10.6, 17.5, 9.8, 8.1, 3.6, and 34.0 % to the coarse fractions, respectively. The contributions of these factors on haze days were higher than those on non-haze days, except for mineral dust and industrial pollution. Additionally, the $R_{H/N}$ of the six sources was highest for SIA (10.7 to fine particles vs. 7.4 to coarse particles), followed by coal combustion (3.2 vs.1.7), primary emissions from vehicles (2.5 vs. 4.1), biomass burning (2.3 vs. 3.5), mineral dust (0.7 vs. 1.0) and, finally, industrial pollution (0.6 vs. 0.6). The high $R_{H/N}$ values indicated that enhanced secondary conversion might occur in the atmosphere

ACPD
15, 9405–9443, 2015

during heavy-pollution days. Furthermore, primary particles and gaseous precursors from coal combustion and traffic emissions played important roles in haze pollution.

The strong contribution of mineral dust on non-haze days was primarily due to high wind speeds, which transported large quantities of particles from areas outside of, but still near, the city. Similarly, the industrial pollution affecting urban Beijing primarily arose from the surrounding areas, and the high wind speeds on non-haze days transported large quantities of industrial emission particles into Beijing from outside areas. However, on haze days, particles from coal combustion, primary emissions from vehicles, biomass burning and secondary formation were important. Thus, strict control over particles and gaseous precursor emissions from coal and oil combustion is required.

4.3.3 Difference among the size fractions

To gain additional insight into aerosol sources, data for nine size fractions were analyzed to obtain information on the source apportionment. Figure 7 shows that the relative contributions of each identified source varied substantially by size fraction. Among the six sources, SIA and mineral dust, which were also identified in the mass closure analyses, exhibited relative orders in the nine size fractions that were similar to those in the mass closure results. However, the contributions of SIA in the nine size fractions differ from SNA obtained by mass closure in terms of values (i.e., 8.2–27.7 for SIA vs. 4.1–34.5 % for SNA). The contribution of mineral dust increased with particle size, with the highest contribution found in the 4.7–5.8 µm fraction (26.6 %) and the lowest in the < 0.43 µm fraction (4.9 %). These results were consistent with the mass closure results, indirectly verifying the reliability of the PMF results.

The contributions of the other four sources generally decreased with increasing size fraction; however, they exhibited high values in the fine and coarse modes. For example, the contributions of primary emissions from vehicles to the total mass in different size fractions ranged from 2.8 to 13.7 %, with the highest proportion found in the 0.65–1.1 µm fraction (13.7 %) and a relatively high proportion found in the 4.7–

ACPD
15, 9405–9443, 2015

5.8 µm fraction (10.0 %). Similarly, the contributions of coal combustion ranged from 20.2 (4.7–5.8 µm) to 31.7 % (< 0.43 µm), and the second highest proportion (27.8 %) appeared in the coarse mode (3.3–4.7 µm). The contributions of industrial pollution and biomass burning were approximately 6 and 7 %, respectively, with high proportions in the fine (< 0.43 µm) and coarse fractions (3.3–4.7 and 4.7–5.8 µm). The complexity of the source apportionment result for different size fractions indirectly verifies that the source apportionment of $PM_{2.5}$ cannot provide comprehensive source information because it neglects the importance of the sources that dominated the coarse size fractions. For example, the highest proportion of industrial pollution was observed in the size fraction of 3.3–4.7 µm.

To further examine the importance of source apportionment in the different size fractions, we compared the source apportionment results for the corresponding size subfractions within $PM_{2.1}$ and $PM_{2.1-9}$. As shown in Fig. 7, the contributions of each source to PM significantly varied among the size fractions within $PM_{2.1}$ and $PM_{2.1-9}$. The contributions of mineral dust, SIA and industrial pollution to size fractions within $PM_{2.1}$ ranged from 4.9 to 11.2 %, from 17.6 to 27.7 % and from 3.6 to 7.4 %, respectively. In addition, significant differences were observed among the size fractions within $PM_{2.1-9}$ for the contributions of primary emissions from vehicles and SIA, which ranged from 2.8 to 10.0 % and from 8.2 to 18.4 %, respectively. This result further indicated the importance of source apportionment for subdivided size fractions within $PM_{2.1}$ and $PM_{2.1-9}$.

4.3.4 Back trajectory cluster

It was estimated that approximately 34 % of $PM_{2.5}$ on average in urban Beijing can be attributed to sources outside Beijing, and the contribution increased 50–70 % during sustained wind flow from the south Hebei Province (Streets et al., 2007). This modeling result indicated the importance of the regional transport effect on fine particles in urban Beijing, but the source apportionment based on size-resolved chemical measurements remained unavailable until now.

ACPD
15, 9405–9443, 2015

To fill this gap, the annual data were subjected to back trajectory cluster analysis to identify source regions and the primary atmospheric circulation pathways that influence the PM concentration and the chemical species (Fig. 8). The air masses that reach Beijing follow seven main paths, including four from the NW (C1, C2, C5 and C7) and one each from the SW (C3), SE (C4) and NE (C6). Figure S4 shows the size distributions of the mass concentrations within each trajectory cluster. The size distributions of the mass concentrations reveal large differences between the different trajectory clusters in the fine mode, especially in the peak size fraction (0.65–1.1 µm).

Because regional transport has a stronger effect on fine particles than on coarse particles and the largest differences were found between trajectory clusters, we only report the identified sources in $PM_{2.1}$ associated with different trajectory clusters to examine the effect of the different source regions (Fig. 8). The polluted air mass trajectories are defined as those with $PM_{2.1}$ concentrations higher than the annual mean of 67.3 µg m^{-3}.

Although the greatest proportion (approximately 36 %) of the trajectories were assigned to the NW cluster, this cluster was associated with the lowest $PM_{2.1}$ concentration, 47.6 µg m^{-3}. Thus, this cluster has a weaker effect on PM pollution in Beijing. The long and rapidly moving trajectories were disaggregated into this group, and members of this cluster have extremely long transport patterns in which some parts cross over Mongolia, Inner Mongolia and northwest Hebei. In addition, this cluster was dominated by mineral dust (21.9 %).

The SW cluster is the most important transport pathway; it has a large number of trajectories (approximately 32 %) and a high $PM_{2.1}$ concentration (79.9 µg m^{-3}). The trajectories belonging to the SW cluster are characterized by the shortest trajectories, indicative of the closest and slowest-moving air masses, which are primarily transported from Hebei and south Beijing. Most of the extreme episodes in this group were probably enriched by regional and local emission sources. As shown in Fig. 8, this cluster was dominated by SIA (25.4 %) and coal combustion (22.9 %).

ACPD
15, 9405–9443, 2015

As shown in Fig. 8, only 15 and 16 % of the trajectories were assigned to the SE and NE clusters, respectively. However, these trajectories were associated with high $PM_{2.1}$ concentrations (87.0 and 67.4 $\mu g\,m^{-3}$). The SE cluster typically followed a flow pattern over north Jiangsu and Shandong and was dominated by SIA (40.8 %). The NE cluster, which crossed over the Liaoning Province and Tianjin, was also dominated by SIA (25.8 %) and coal combustion (21.3 %). These results show that southern flows were dominant in urban Beijing and were associated with higher SIA and coal combustion contributions. Because SIA is primarily attributed to the transformation of precursors that originate from oil and coal combustion (i.e., NO_x and SO_2), controlling oil and coal combustion in the southern regions is required.

4.4 Reconstructing the visibility

In addition to the fine and coarse particles, various chemical components play significant but different roles in reducing the visibility on haze days. To further investigate the effect of the chemical species in the different size fractions and meteorological factors on visibility, correlation analysis was performed, and regression models were used in this study.

The results showed that visibility had high correlation coefficients (> 0.5) with SO_4^{2-} in the 0.43–0.65 and 0.65–1.1 µm size fractions, NH_4^+ in 0.43–0.65 µm and NO_3^- in 0.65–1.1 µm size fractions and Ca^{2+} in 5.8–9 µm size fraction as well as the RH and WS. All of the parameters that exert significant effects on visibility were then used as the inputs in multiple linear regression models to simulate the visibility. Ultimately, we developed the following regression equation for urban visibility in Beijing:

$$\begin{aligned}\text{Visibility} = {} & 13.543 - 9.214\text{RH} + 2.069\text{WS} - 0.06[NH_4^+]_{0.43-0.65} - 0.037[SO_4^{2-}]_{0.43-0.65} \\ & - 0.445[SO_4^{2-}]_{0.65-1.1} - 0.186[NO_3^-]_{0.65-1.1} - 2.18[Ca^{2+}]_{5.8-9} \end{aligned} \quad (3)$$

It has been reported that SO_4^{2-}, NO_3^- and NH_4^+ in $PM_{2.5}$ play important roles in the visibility degradation during haze events in Beijing (Zhang et al., 2015). Compared

ACPD
15, 9405–9443, 2015

with previous studies, this study provides additional insight into the effect of chemical species in different size fractions on the visibility. According to the results, the most important factors that affect the visibility were NH_4^+ in the 0.43–0.65 µm size fraction, SO_4^{2-} in the 0.65–1.1 µm size fraction, NO_3^- in the 0.65–1.1 µm size fraction and Ca^{2+} in the 5.8–9 µm size fraction as well as the RH and WS. The species that degrade visibility were primarily accumulated in the submicron particles. Because SO_4^{2-}, NO_3^- and NH_4^+ in this size fraction was primarily from gaseous precursors (NH_3, NO_2 and SO_2), gaseous emission regulatory controls for these precursors are key steps in reducing PM pollution and thereby improving visibility.

Our findings were similar to those reported for Jinan, in which the SO_4^{2-} and water content in the 1.0–1.8 µm fraction and the RH were the most important factors that affected the visibility (Cheng et al., 2011). However, in this study, the Ca^{2+} in the coarse particles, which was primarily from construction dust (Maenhaut et al., 2002), also played an important role in reducing the visibility in urban Beijing. Thus, construction dust must be controlled to improve visibility.

To validate the above equation, datasets from other periods (from March 2012 to February 2013) were used to characterize the relationship between the visibility and the chemical species. As shown in Fig. S5, the estimated visibility correlated well with the measured visibility ($R^2 = 0.62$, $p < 0.05$). However, the ratio of the estimated visibility to the measured visibility was only 0.49, and discrete points primarily appeared for visibilities greater than 15 km. After scaling down, i.e., using datasets with visibilities less than 15 km to validate the above equation, the ratio of the estimated visibility to the measured visibility reached 0.92. This result indicated that the species that reduced the visibility were different in haze and clear conditions. This result is another indication that the above equation can characterize the relationship between visibility and chemical species during haze periods with a visibility of less than 15 km.

ACPD
15, 9405–9443, 2015

5 Summary and conclusions

The analysis of size-segregated airborne particles collected in Beijing from 1 March 2013 to 28 February 2014 was presented. The annual average mass concentrations of the fine and coarse particles were higher than the National Ambient Air Quality Standard (Grade I) of China. The OC, SO_4^{2-}, NO_3^- and NH_4^+ species were the most abundant in the fine particles, accounting for 24.5, 14.7, 11.2 and 9.2 % of the $PM_{2.1}$ mass, respectively. In $PM_{2.1-9}$, the primary chemical components were Ca (16.3 %) and OC (15.5 %). SOC, which formed due to photochemical reactions, primarily accumulated in the "condensation mode". The size distribution of the OC peaked at 0.43–0.65 µm in summer and at 0.65–1.1 µm in winter.

The dataset excluding extreme weather events (i.e., rain, snow and fog) was categorized into non-haze and haze days. NO_3^-, SO_4^{2-}, NH_4^+, Pb, Cd and Tl in $PM_{2.1}$ accumulated heavily during haze periods with $R_{H/N} > 2.4$. In coarse particles, the $R_{H/N}$ values of NO_3^-, SO_4^{2-}, NH_4^+, Pb, Cl^-, Tl, Cd, EC, Na^+, K^+, OC, Mo and Zn were also greater than unity, indicating that the effect of particles with a diameter larger than 2.1 µm cannot be neglected. The annual average size distributions of SO_4^{2-}, OC, NO_3^-, NH_4^+, Cl^-, K^+ and Cu exhibited peak shifts from 0.43–0.65 µm on non-haze days to 0.65–1.1 µm on haze days. In addition, a regression equation (Visibility = $13.543 - 9.214RH + 2.069WS - 0.06[NH_4^+]_{0.43-0.65} - 0.037[SO_4^{2-}]_{0.43-0.65} - 0.445[SO_4^{2-}]_{0.65-1.1} - 0.186[NO_3^-]_{0.65-1.1} - 2.18[Ca^{2+}]_{5.8-9}$) was developed to characterize the relationship between the visibility and the chemical species concentrations when the visibility was less than 15 km.

The mass closure results showed that OM, SNA and CM dominated the fine and coarse particulate mass concentrations. Although OM dominates in fine particles, it decreased from 37.9 % on non-haze days to 33.0 % on haze days. In contrast, the contribution of SNA to the $PM_{2.1}$ mass increased from 19.1 % on non-haze days to 32.3 % on haze days, indicating that SNA played a key role in haze formation. Moreover, the SNA, OM, HM and EC contributions decreased as the size increased, whereas those

ACPD
15, 9405–9443, 2015

of CM and SS exhibited the opposite trend. Further studies are required to determine the identities of the unidentified components in the larger size fractions.

Six sources were identified using the PMF method based on the annual $PM_{2.1}$, $PM_{2.1-9}$ and size-segregated data. The source concentrations varied between non-haze and haze days. The results show that coal combustion, primary emissions from vehicles, biomass burning and secondary formation were major contributors on haze days. In contrast, mineral dust and industrial pollution were important sources on non-haze days. In addition, the relative contributions of these sources in Beijing varied significantly as the fraction sizes changed. The contributions of all of the sources decreased as the size of the fraction increased with the exception of mineral dust; however, they exhibited relatively high proportions in the fine and coarse modes, indicating the importance of source apportionment for size sub-fractions within $PM_{2.1}$ and $PM_{2.1-9}$. Combining these findings with the trajectory clustering results, the source regions associated with $PM_{2.1}$ in Beijing were further explored. We found that the southern and northeastern flows are associated with greater SIA and coal combustion contributions, whereas the northwestern flows transport more mineral dust.

The Supplement related to this article is available online at doi:10.5194/acpd-15-9405-2015-supplement.

Acknowledgements. This study supported by the "Strategic Priority Research Program" of the Chinese Academy of Sciences (XDB05020000 and XDA05100100), the National Natural Science Foundation of China (No.:41405144, 41230642 and 41321064), and Haze Observation Project Especially for Jing-Jin-Ji Area (HOPE-J^{3}A) (No.:KJZD-EW-TZ-G06-01-04).

ACPD
15, 9405–9443, 2015

References

Bullock, K. R., Duvall, R. M., Norris, G. A., McDow, S. R., and Hays, M. D.: Evaluation of the CMB and PMF models using organic molecular markers in fine particulate matter collected during the Pittsburgh Air Quality Study, Atmos. Environ., 42, 6897–6904, doi:10.1016/j.atmosenv.2008.05.011, 2008.

Cao, J., Lee, S., Chow, J. C., Watson, J. G., Ho, K., Zhang, R., Jin, Z., Shen, Z., Chen, G., and Kang, Y.: Spatial and seasonal distributions of carbonaceous aerosols over China, J. Geophys. Res. D., 112, D22S11, doi:10.1029/2006JD008205, 2007.

Chan, C. Y., Xu, X. D., Li, Y. S., Wong, K. H., Ding, G. A., Chan, L. Y., and Cheng, X. H.: Characteristics of vertical profiles and sources of $PM_{2.5}$, PM_{10} and carbonaceous species in Beijing, Atmos. Environ., 39, 5113–5124, doi:10.1016/j.atmosenv.2005.05.009, 2005.

Cheng, S.-H., Yang, L.-X., Zhou, X.-H., Xue, L.-K., Gao, X.-M., Zhou, Y., and Wang, W.-X.: Size-fractionated water-soluble ions, situ pH and water content in aerosol on hazy days and the influences on visibility impairment in Jinan, China, Atmos. Environ., 45, 4631–4640, doi:10.1016/j.atmosenv.2011.05.057, 2011.

Cheng, Y., Engling, G., He, K.-B., Duan, F.-K., Du, Z.-Y., Ma, Y.-L., Liang, L.-L., Lu, Z.-F., Liu, J.-M., Zheng, M., and Weber, R. J.: The characteristics of Beijing aerosol during two distinct episodes: impacts of biomass burning and fireworks, Environ. Pollut., 185, 149–157, doi:10.1016/j.envpol.2013.10.037, 2014.

Contini, D., Cesari, D., Genga, A., Siciliano, M., Ielpo, P., Guascito, M. R., and Conte, M.: Source apportionment of size-segregated atmospheric particles based on the major water-soluble components in Lecce (Italy), Sci. Total. Environ., 472, 248–261, doi:10.1016/j.scitotenv.2013.10.127, 2014.

Du, H., Kong, L., Cheng, T., Chen, J., Du, J., Li, L., Xia, X., Leng, C., and Huang, G.: Insights into summertime haze pollution events over Shanghai based on online water-soluble ionic composition of aerosols, Atmos. Environ., 45, 5131–5137, doi:10.1016/j.atmosenv.2011.06.027, 2011.

Du, Z., He, K., Cheng, Y., Duan, F., Ma, Y., Liu, J., Zhang, X., Zheng, M., and Weber, R.: A year long study of water-soluble organic carbon in Beijing II: light absorption properties, Atmos. Environ., 89, 235–241, doi:10.1016/j.atmosenv.2014.02.022, 2014.

ACPD
15, 9405–9443, 2015

Duan, F., He, K., Ma, Y., Jia, Y., Yang, F., Lei, Y., Tanaka, S., and Okuta, T.: Characteristics of carbonaceous aerosols in Beijing, China, Chemosphere, 60, 355–364, doi:10.1016/j.chemosphere.2004.12.035, 2005.

Duarte, R. M. B. O., Mieiro, C. L., Penetra, A., Pio, C. A., and Duarte, A. C.: Carbonaceous materials in size-segregated atmospheric aerosols from urban and coastal-rural areas at the Western European Coast, Atmos. Res., 90, 253–263, doi:10.1016/j.atmosres.2008.03.003, 2008.

Gao, J., Chai, F., Wang, T., Wang, S., and Wang, W.: Particle number size distribution and new particle formation: new characteristics during the special pollution control period in Beijing, J. Environ. Sci., 24, 14–21, doi:10.1016/S1001-0742(11)60725-0, 2012.

Guo, S., Hu, M., Zamora, M. L., Peng, J., Shang, D., Zheng, J., Du, Z., Wu, Z., Shao, M., Zeng, L., Molina, M. J., and Zhang, R.: Elucidating severe urban haze formation in China, P. Natl. Acad. Sci. USA, 111, 17373–17378, doi:10.1073/pnas.1419604111, 2014.

Huang, R. J., Zhang, Y. L., Bozzetti, C., Ho, K. F., Cao, J. J., Han, Y. M., Daellenbach, K. R., Slowik, J. G., Platt, S. M., Canonaco, F., Zotter, P., Wolf, R., Pieber, S. M., Bruns, E. A., Crippa, M., Ciarelli, G., Piazzalunga, A., Schwikowski, M., Abbaszade, G., Schnelle-Kreis, J., Zimmermann, R., An, Z. S., Szidat, S., Baltensperger, U., El Haddad, I., and Prevot, A. S. H.: High secondary aerosol contribution to particulate pollution during haze events in China, Nature, 514, 218–222, doi:10.1038/nature13774, 2014.

Hueglin, C., Gehrig, R., Baltensperger, U., Gysel, M., Monn, C., and Vonmont, H.: Chemical characterisation of $PM_{2.5}$, PM_{10} and coarse particles at urban, near-city and rural sites in Switzerland, Atmos. Environ., 39, 637–651, doi:10.1016/j.atmosenv.2004.10.027, 2005.

Jing, H., Li, Y.-F., Zhao, J., Li, B., Sun, J., Chen, R., Gao, Y., and Chen, C.: Wide-range particle characterization and elemental concentration in Beijing aerosol during the 2013 Spring Festival, Environ. Pollut., 192, 204–211, doi:10.1016/j.envpol.2014.06.003, 2014.

Karanasiou, A. A., Siskos, P. A., and Eleftheriadis, K.: Assessment of source apportionment by Positive Matrix Factorization analysis on fine and coarse urban aerosol size fractions, Atmos. Environ., 43, 3385–3395, doi:10.1016/j.atmosenv.2009.03.051, 2009.

Karnae, S. and John, K.: Source apportionment of fine particulate matter measured in an industrialized coastal urban area of South Texas, Atmos. Environ., 45, 3769–3776, doi:10.1016/j.atmosenv.2011.04.040, 2011.

ACPD
15, 9405–9443, 2015

Li, X., Wang, L., Wang, Y., Wen, T., Yang, Y., Zhao, Y., and Wang, Y.: Chemical composition and size distribution of airborne particulate matters in Beijing during the 2008 Olympics, Atmos. Environ., 50, 278–286, doi:10.1016/j.atmosenv.2011.12.021, 2012a.
Li, X., Wang, L., Wang, Y., Wen, T., Yang, Y., Zhao, Y., and Wang, Y.: Chemical composition and size distribution of airborne particulate matters in Beijing during the 2008 Olympics, Atmos. Environ., 50, 278–286, doi:10.1016/j.atmosenv.2011.12.021, 2012b.
Li, X., Wang, L., Ji, D., Wen, T., Pan, Y., Sun, Y., and Wang, Y.: Characterization of the size-segregated water-soluble inorganic ions in the Jing-Jin-Ji urban agglomeration: spatial/temporal variability, size distribution and sources, Atmos. Environ., 77, 250–259, doi:10.1016/j.atmosenv.2013.03.042, 2013.
Liu, S., Hu, M., Slanina, S., He, L.-Y., Niu, Y.-W., Bruegemann, E., Gnauk, T., and Herrmann, H.: Size distribution and source analysis of ionic compositions of aerosols in polluted periods at Xinken in Pearl River Delta (PRD) of China, Atmos. Environ., 42, 6284–6295, doi:10.1016/j.atmosenv.2007.12.035, 2008.
Liu, Z. R., Hu, B., Liu, Q., Sun, Y., and Wang, Y. S.: Source apportionment of urban fine particle number concentration during summertime in Beijing, Atmos. Environ., 96, 359–369, doi:10.1016/j.atmosenv.2014.06.055, 2014.
Maenhaut, W., Cafmeyer, J., Dubtsov, S., and Chi, X.: Detailed mass size distributions of elements and species, and aerosol chemical mass closure during fall 1999 at Gent, Belgium, Nucl. Instrum. Methods, 189, 238–242, doi:10.1016/s0168-583x(01)01049-7, 2002.
McFiggans, G.: ATMOSPHERIC SCIENCE Involatile particles from rapid oxidation, Nature, 506, 442–443, doi:10.1038/506442a, 2014.
Moon, K. J., Han, J. S., Ghim, Y. S., and Kim, Y. J.: Source apportionment of fine carbonaceous particles by positive matrix factorization at Gosan background site in East Asia, Environ. Int., 34, 654–664, doi:10.1016/j.envint.2007.12.021, 2008.
Pan, Y. P. and Wang, Y. S.: Atmospheric wet and dry deposition of trace elements at 10 sites in Northern China, Atmos. Chem. Phys., 15, 951–972, doi:10.5194/acp-15-951-2015, 2015.
Pan, Y. P., Wang, Y. S., Tang, G. Q., and Wu, D.: Spatial distribution and temporal variations of atmospheric sulfur deposition in Northern China: insights into the potential acidification risks, Atmos. Chem. Phys., 13, 1675–1688, doi:10.5194/acp-13-1675-2013, 2013.
Pant, P. and Harrison, R. M.: Critical review of receptor modelling for particulate matter: a case study of India, Atmos. Environ., 49, 1–12, doi:10.1016/j.atmosenv.2011.11.060, 2012.

ACPD
15, 9405–9443, 2015

Pillai, P. S. and Moorthy, K. K.: Aerosol mass-size distributions at a tropical coastal environment: response to mesoscale and synoptic processes, Atmos. Environ., 35, 4099–4112, doi:10.1016/s1352-2310(01)00211-4, 2001.

Schleicher, N., Norra, S., Fricker, M., Kaminski, U., Chen, Y., Chai, F., Wang, S., Yu, Y., and Cen, K.: Spatio-temporal variations of black carbon concentrations in the Megacity Beijing, Environ. Pollut., 182, 392–401, doi:10.1016/j.envpol.2013.07.042, 2013.

Sirois, A. and Bottenheim, J. W.: Use of backward trajectories to interpret the 5-year record of PAN and O_3 ambient air concentrations at Kejimkujik National Park, Nova Scotia, J. Geophys. Res., 100, 2867–2881, doi:10.1029/94jd02951, 1995.

Song, Y., Zhang, Y., Xie, S., Zeng, L., Zheng, M., Salmon, L. G., Shao, M., and Slanina, S.: Source apportionment of $PM_{2.5}$ in Beijing by positive matrix factorization, Atmos. Environ., 40, 1526–1537, doi:10.1016/j.atmosenv.2005.10.039, 2006.

Streets, D. G., Fu, J. S., Jang, C. J., Hao, J., He, K., Tang, X., Zhang, Y., Wang, Z., Li, Z., Zhang, Q., Wang, L., Wang, B., and Yu, C.: Air quality during the 2008 Beijing Olympic Games, Atmos. Environ., 41, 480–492, doi:10.1016/j.atmosenv.2006.08.046, 2007.

Sun, J., Zhang, Q., Canagaratna, M. R., Zhang, Y., Ng, N. L., Sun, Y., Jayne, J. T., Zhang, X., Zhang, X., and Worsnop, D. R.: Highly time- and size-resolved characterization of submicron aerosol particles in Beijing using an Aerodyne Aerosol Mass Spectrometer, Atmos. Environ., 44, 131–140, doi:10.1016/j.atmosenv.2009.03.020, 2010.

Sun, Y., Zhuang, G., Wang, Y., Han, L., Guo, J., Dan, M., Zhang, W., Wang, Z., and Hao, Z.: The air-borne particulate pollution in Beijing – concentration, composition, distribution and sources, Atmos. Environ., 38, 5991–6004, doi:10.1016/j.atmosenv.2004.07.009, 2004.

Sun, Z., Mu, Y., Liu, Y., and Shao, L.: A comparison study on airborne particles during haze days and non-haze days in Beijing, Sci. Total Environ., 456–457, 1–8, doi:10.1016/j.scitotenv.2013.03.006, 2013.

Tian, S., Pan, Y., Liu, Z., Wen, T., and Wang, Y.: Size-resolved aerosol chemical analysis of extreme haze pollution events during early 2013 in urban Beijing, China, J. Hazard. Mater., 279, 452–460, doi:10.1016/j.jhazmat.2014.07.023, 2014.

Titos, G., Lyamani, H., Pandolfi, M., Alastuey, A., and Alados-Arboledas, L.: Identification of fine (PM_1) and coarse (PM_{10-1}) sources of particulate matter in an urban environment, Atmos. Environ., 89, 593–602, doi:10.1016/j.atmosenv.2014.03.001, 2014.

Wang, L. T., Wei, Z., Yang, J., Zhang, Y., Zhang, F. F., Su, J., Meng, C. C., and Zhang, Q.: The 2013 severe haze over southern Hebei, China: model evaluation, source apportionment, and

ACPD
15, 9405–9443, 2015

policy implications, Atmos. Chem. Phys., 14, 3151–3173, doi:10.5194/acp-14-3151-2014, 2014.
Wang, X., Wang, W., Yang, L., Gao, X., Nie, W., Yu, Y., Xu, P., Zhou, Y., and Wang, Z.: The secondary formation of inorganic aerosols in the droplet mode through heterogeneous aqueous reactions under haze conditions, Atmos. Environ., 63, 68–76, doi:10.1016/j.atmosenv.2012.09.029, 2012.
Wang, Y. Q., Zhang, X. Y., and Arimoto, R.: The contribution from distant dust sources to the atmospheric particulate matter loadings at XiAn, China during spring, Sci. Total Environ., 368, 875–883, doi:10.1016/j.scitotenv.2006.03.040, 2006.
Yang, L., Cheng, S., Wang, X., Nie, W., Xu, P., Gao, X., Yuan, C., and Wang, W.: Source identification and health impact of $PM_{2.5}$ in a heavily polluted urban atmosphere in China, Atmos. Environ., 75, 265–269, doi:10.1016/j.atmosenv.2013.04.058, 2013.
Yang, X., Chen, Y. Z., Liu, H. F., Zhao, Y. X., Gao, J., Chai, F. H., and Meng, F.: Characteristics and formation mechanism of a serious haze event in January 2013 in Beijing, China, Environm. Sci., 34, 282–288, 2014.
Yang, Y., Wang, Y., Wen, T., Wei, L., Ya'nan, Z., and Liang, L.: Elemental composition of $PM_{2.5}$ and PM_{10} at Mount Gongga in China during 2006, Atmos. Res., 93, 801–810, doi:10.1016/j.atmosres.2009.03.014, 2009.
Yao, X., Lau, A. P. S., Fang, M., Chan, C. K., and Hu, M.: Size distributions and formation of ionic species in atmospheric particulate pollutants in Beijing, China: inorganic ions, Atmos. Environ., 37, 2991–3000, doi:10.1016/S1352-2310(03)00255-3, 2003.
Zhang, G., Bi, X., Chan, L. Y., Wang, X., Sheng, G., and Fu, J.: Size-segregated chemical characteristics of aerosol during haze in an urban area of the Pearl River Delta region, China, Urban. Clim., 4, 74–84, doi:10.1016/j.uclim.2013.05.002, 2013.
Zhang, J. K., Sun, Y., Liu, Z. R., Ji, D. S., Hu, B., Liu, Q., and Wang, Y. S.: Characterization of submicron aerosols during a month of serious pollution in Beijing, 2013, Atmos. Chem. Phys., 14, 2887–2903, doi:10.5194/acp-14-2887-2014, 2014.
Zhang, Q., Quan, J., Tie, X., Li, X., Liu, Q., Gao, Y., and Zhao, D.: Effects of meteorology and secondary particle formation on visibility during heavy haze events in Beijing, China, Sci. Total Environ., 502, 578–584, doi:10.1016/j.scitotenv.2014.09.079, 2015.
Zhang, R., Jing, J., Tao, J., Hsu, S.-C., Wang, G., Cao, J., Lee, C. S. L., Zhu, L., Chen, Z., Zhao, Y., and Shen, Z.: Chemical characterization and source apportionment of $PM_{2.5}$ in

ACPD
15, 9405–9443, 2015

Beijing: seasonal perspective, Atmos. Chem. Phys., 13, 7053–7074, doi:10.5194/acp-13-7053-2013, 2013.
Zhang, W., Zhuang, G., Guo, J., Xu, D., Wang, W., Baumgardner, D., Wu, Z., and Yang, W.: Sources of aerosol as determined from elemental composition and size distributions in Beijing, Atmos. Res., 95, 197–209, doi:10.1016/j.atmosres.2009.09.017, 2010.
Zhang, X. Y., Wang, Y. Q., Zhang, X. C., Guo, W., and Gong, S. L.: Carbonaceous aerosol composition over various regions of China during 2006, J. Geophys. Res., 113, D14111, doi:10.1029/2007jd009525, 2008.

ACPD
15, 9405–9443, 2015

Table 1. Concentrations of different chemical compositions in size-resolved particles during entire sampling period (annual) and four seasons ($\mu g\,m^{-3}$).

	Annual		Spring		Summer		Autumn		Winter	
Size	$PM_{2.1}$	$PM_{2.1-9}$	$PM_{2.1}$	$PM_{2.1-9}$	$PM_{2.1}$	$PM_{2.1-9}$	$PM_{2.1}$	$PM_{2.1-9}$	$PM_{2.1}$	$PM_{2.1-9}$
Mass	67.27	62.33	64.65	68.05	65.05	57.97	62.52	62.87	76.84	60.41
OC	16.50	9.63	16.26	10.44	20.19	16.68	13.40	6.76	16.16	4.64
EC	2.01	0.77	1.28	0.71	1.47	0.81	1.99	0.82	3.32	0.75
Na^+	0.79	0.66	0.48	0.57	0.27	0.31	1.67	0.92	0.74	0.82
NH_4^+	6.17	0.70	8.00	0.74	6.11	0.41	4.65	0.56	5.92	1.08
K^+	0.72	0.29	0.83	0.49	0.33	0.12	0.60	0.09	1.12	0.46
Mg^{2+}	0.21	0.40	0.30	0.41	0.14	0.36	0.20	0.42	0.20	0.40
Ca^{2+}	1.01	3.38	1.25	3.98	0.67	2.69	1.00	3.77	1.10	3.08
Cl^-	1.58	0.81	1.98	1.19	0.17	0.31	1.23	0.46	2.95	1.28
NO_3^-	7.51	2.78	8.51	3.56	4.08	2.33	6.60	2.46	10.84	2.76
SO_4^{2-}	9.87	2.17	11.02	2.80	10.02	1.47	9.28	2.08	9.16	2.35
Na	1.78	1.34	1.77	1.33	1.81	1.12	1.81	1.29	1.73	1.64
Mg	0.45	1.19	0.51	1.63	0.49	1.08	0.46	1.14	0.35	0.91
Al	0.65	1.39	0.73	2.06	0.60	0.90	0.69	1.32	0.59	1.29
K	0.69	0.62	0.88	0.98	0.49	0.49	0.74	0.59	0.65	0.42
Ca	3.54	10.17	4.03	16.31	4.63	10.20	3.21	8.63	2.30	5.55
V	0.10	0.05	0.07	0.02	0.06	0.02	0.14	0.08	0.15	0.08
Cr	0.36	0.18	0.25	0.07	0.21	0.07	0.48	0.30	0.50	0.29
Mn	0.04	0.04	0.05	0.06	0.03	0.03	0.04	0.04	0.03	0.04
Fe	1.23	2.58	1.55	3.66	1.43	2.08	1.36	2.62	0.58	1.98
Co	0.001	0.001	0.001	0.001	0.001	0.001	0.001	0.001	0.001	0.001
Ni	0.013	0.014	0.011	0.012	0.014	0.010	0.014	0.018	0.014	0.015
Cu	0.026	0.020	0.030	0.020	0.015	0.015	0.029	0.022	0.029	0.023
Zn	0.21	0.10	0.24	0.12	0.18	0.09	0.23	0.09	0.19	0.09
As	0.010	0.006	0.008	0.002	0.008	0.005	0.010	0.007	0.014	0.013
Mo	0.006	0.006	0.002	0.001	0.002	0.002	0.002	0.001	0.002	0.002
Cd	0.001	0.000	0.001	0.000	0.001	0.000	0.001	0.000	0.001	0.000
Ba	0.017	0.043	0.018	0.057	0.014	0.032	0.018	0.044	0.017	0.039
Tl	0.001	0.000	0.001	0.000	0.001	0.000	0.001	0.000	0.001	0.000
Pb	0.089	0.018	0.094	0.022	0.071	0.013	0.088	0.015	0.103	0.022
Th	0.000	0.000	0.000	0.001	0.000	0.000	0.000	0.000	0.000	0.001
U	0.000	0.000	0.000	0.000	0.000	0.000	0.000	0.000	0.000	0.000

ACPD
15, 9405–9443, 2015

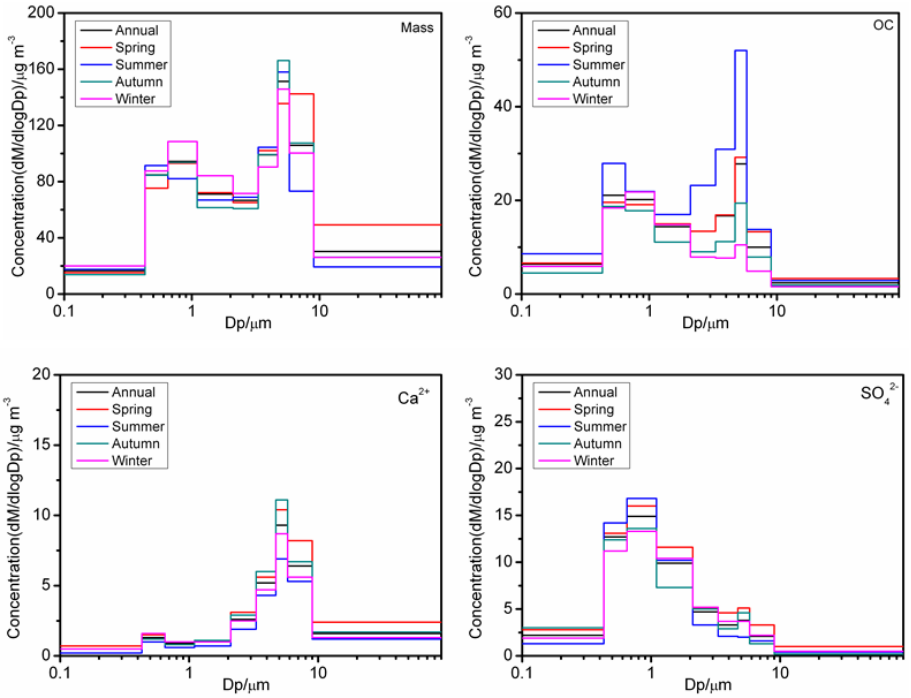

Figure 1. Mass concentration size distributions and that of typical chemical species in different categories.

ACPD
15, 9405–9443, 2015

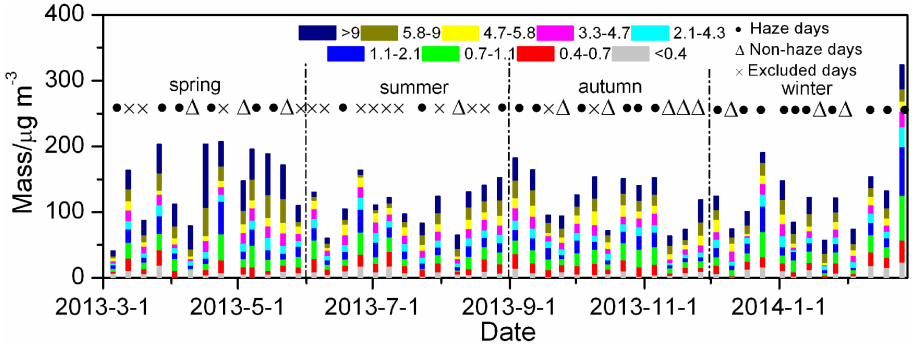

Figure 2. Size-resolved mass concentration (distributions that are marked as solid circle and open triangle denote haze and non-haze days, respectively).

ACPD
15, 9405–9443, 2015

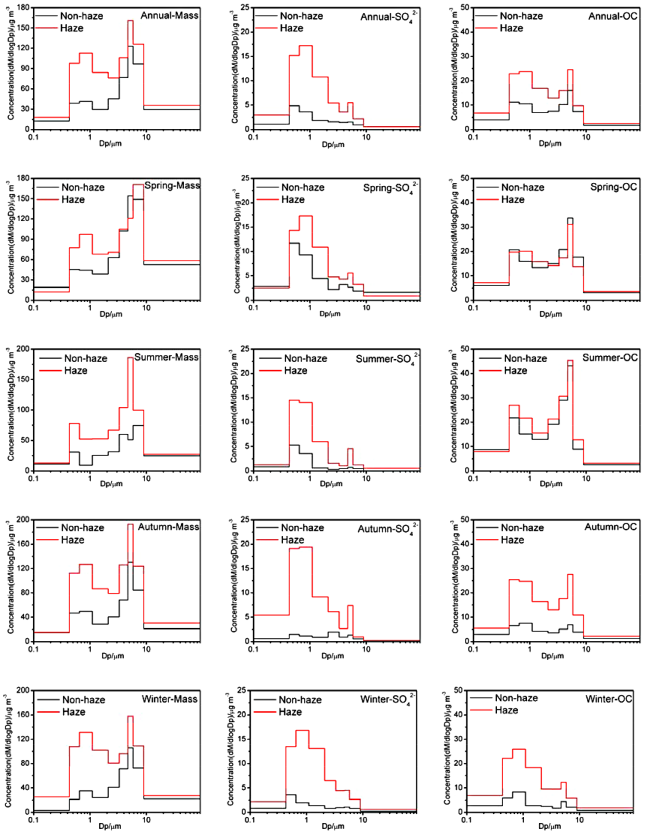

Figure 3. Mass concentration size distributions on haze and non-haze days over the entire sampling period (annual) and by season as well as that of the typical chemical species.

ACPD
15, 9405–9443, 2015

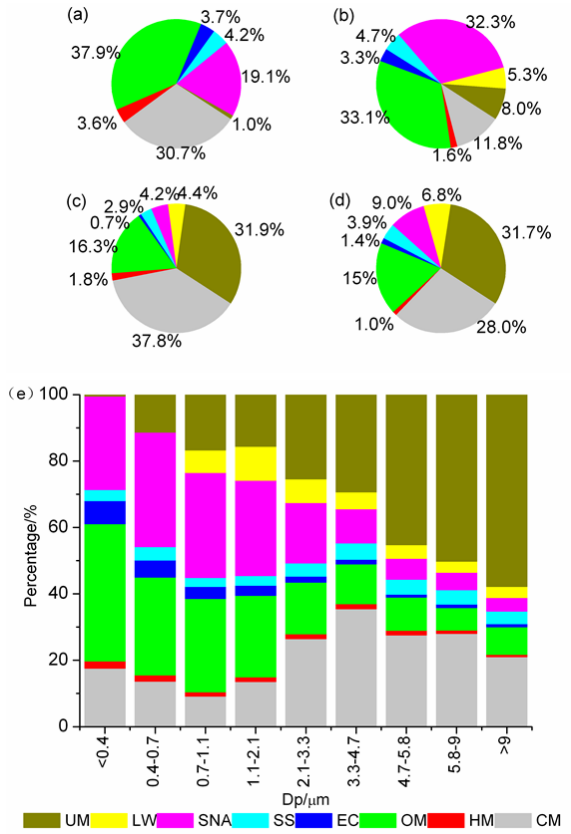

Figure 4. Contributions of different components to the total masses in **(a)** $PM_{2.1}$ on non-haze days; **(b)** $PM_{2.1}$ on haze days; **(c)** $PM_{2.1-9}$ on non-haze days; **(d)** $PM_{2.1-9}$ on haze days; **(e)** different size fractions.

ACPD
15, 9405–9443, 2015

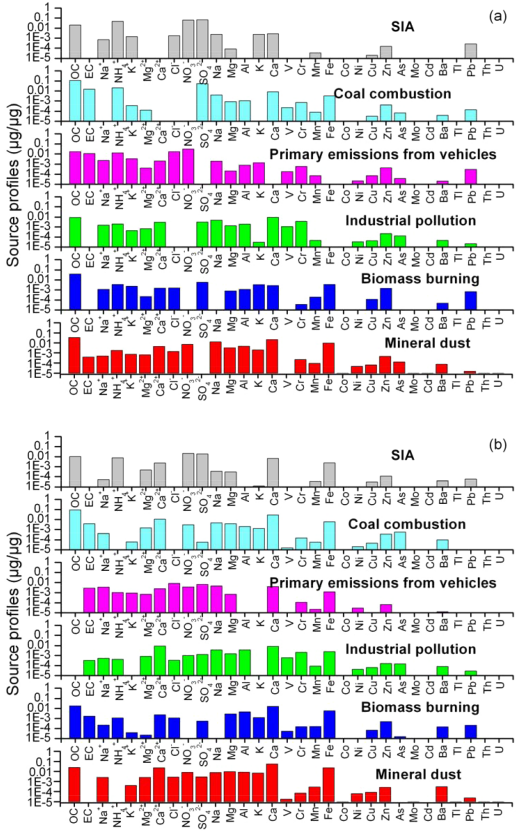

Figure 5. The profiles of each source in **(a)** fine and **(b)** coarse fractions.

ACPD
15, 9405–9443, 2015

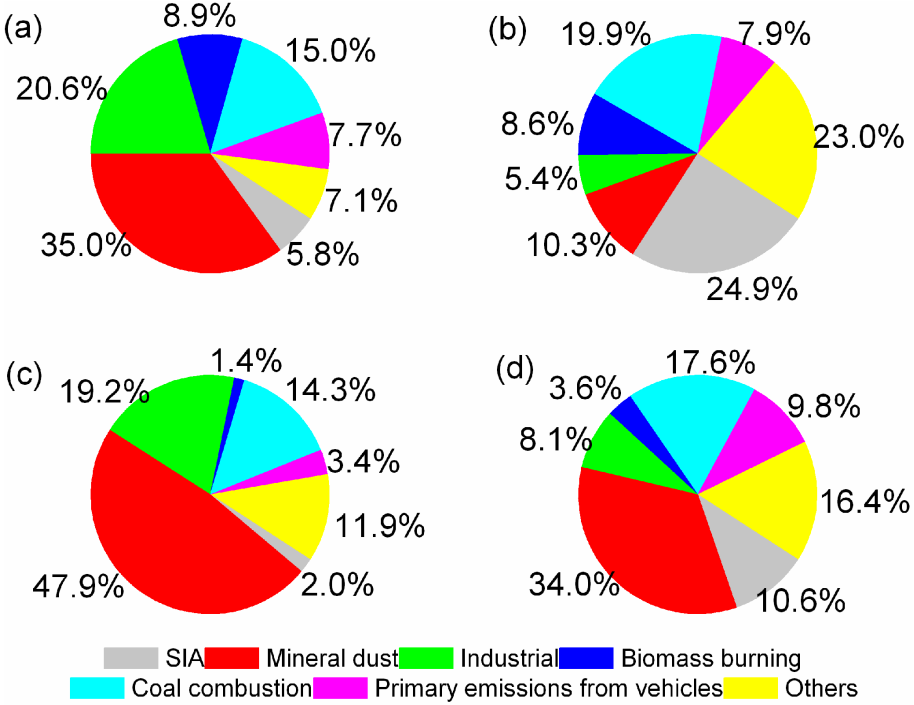

Figure 6. Relative contributions from each identified source to **(a)** $PM_{2.1}$ on non-haze days; **(b)** $PM_{2.1}$ on haze days; **(c)** $PM_{2.1-9}$ on non-haze days; **(d)** $PM_{2.1-9}$ on haze days.

ACPD
15, 9405–9443, 2015

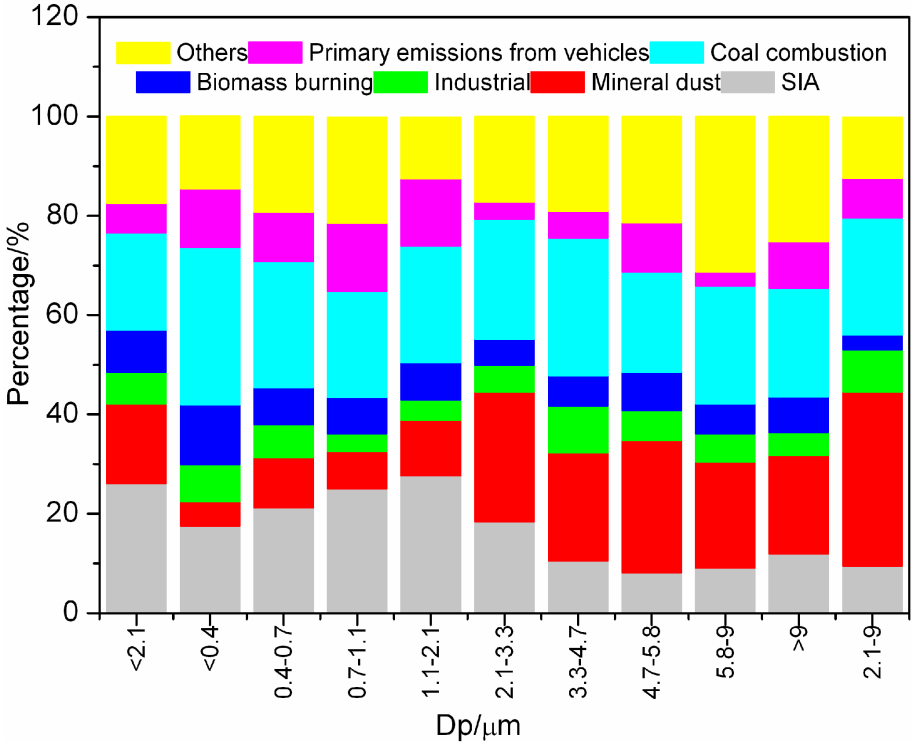

Figure 7. Relative contributions from each identified source to different size fractions.

ACPD
15, 9405–9443, 2015

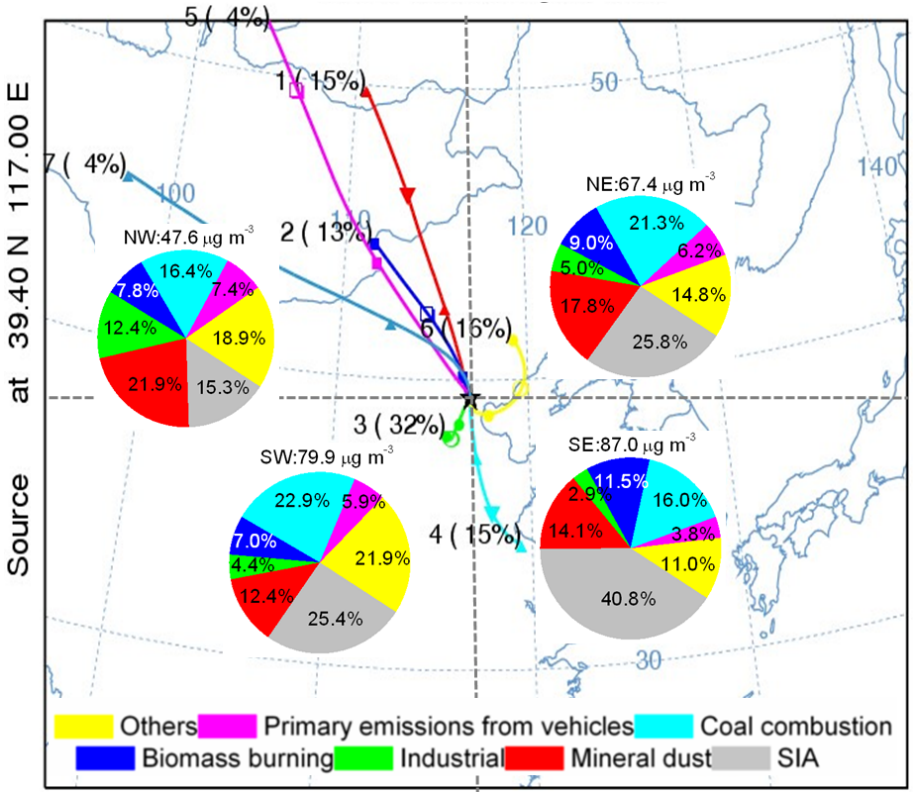

Figure 8. Relative contributions from each identified source to $PM_{2.1}$ at different trajectory clusters.

ACPD
15, 9405–9443, 2015